Integrating Materials and Manufacturing Innovation (2025) 14:573–592
https://doi.org/10.1007/s40192-025-00427-0

THEMATIC SECTION: 8TH WORLD CONGRESS ON INTEGRATED COMPUTATIONAL MATERIALS ENGINEERING

Efficient Multiscale Simulations of Incremental Sheet Forming Using Machine Learning Surrogate Models for Crystal Plasticity

John S. Weeks[1] · **Aaron P. Stebner**[1]

Received: 28 August 2025 / Accepted: 15 October 2025 / Published online: 14 November 2025

Abstract
Multiscale crystal plasticity modeling of metal forming offers potential for effective design processes that consider microstructural evolution during significant plastic deformation. However, conventional multiscale methods for forming are expensive due to complex loading conditions and high-cost microscale models, making them challenging to apply in practice. These methods can be significantly accelerated through use of low-cost machine learning surrogate models for the microscale response. While these techniques have been demonstrated for simple load cases, they have not yet been demonstrated for manufacturing applications with full-field texture results. In this work, we develop efficient multiscale simulation workflows for manufacturing through single-point incremental forming using recurrent neural networks for constitutive response and texture evolution of a crystal plasticity model. This approach achieves up to a 63.6x increase in speed compared to conventional techniques and is demonstrated for an aluminum alloy with two unique forming paths. These workflows yield consistent trends between forming force and thickness variation, texture results in agreement with ground truth models, and permit extraction of the full-field texture evolution over the entire formed part. This enables efficient multiscale trade studies and optimization of local microstructures in industrial forming applications.

Keywords Multiscale modeling · Crystal plasticity · Single-point incremental forming · Machine learning · Surrogate modeling

Introduction

Engineering design spaces that assume uniform material properties can be significantly expanded by considering variation of local properties throughout a component. This is a key concept in *metamorphic manufacturing* (MM), a manufacturing approach that uses numerically controlled incremental deformations to achieve complex shapes and tailored local properties [1]. Computational modeling techniques are necessary for realization of MM in order to understand the correlation between local and global properties, and the processing conditions before, during, and after manufacturing operations. In the context of metal forming, local scales manifest as sections of spatially-distinct microstructures and global scales arise from boundary conditions of the manufacturing process. Integrated Computational Materials Engineering (ICME) and multiscale modeling focus on coupling models across length scales such as these [2], however, nonlinear behavior during forming makes these approaches expensive [3]. Therefore, development of efficient, multiscale models is necessary to enable MM techniques. In this work, we demonstrate an efficient multiscale simulation workflow of an incremental deformation strategy called incremental sheet forming.

Incremental sheet forming (ISF) is a metal manufacturing technology that uses a numerically controlled tool to incrementally deform sheet metal into a final geometry by tracing a pre-defined path [4]. The simplest strategy of ISF is single-point incremental forming (SPIF) which uses a single hemispherical tool. Variations of SPIF have been developed to improve geometric accuracy such two-point incremental forming which uses a single tool and secondary die, and double-sided incremental forming (DSIF) which uses two tools

✉ John S. Weeks
jsweeks@gatech.edu

[1] Georgia Tech Manufacturing Institute, Georgia Institute of Technology, 813 Ferst Drive, N.W., Atlanta, GA 30332, USA

on opposing sides of the workpiece [5]. Tool path variation has also been explored by traveling inwards-to-outwards in accumulated double-sided incremental forming [6] and reforming paths over previously formed sections [7]. The existence of various techniques and strategies demonstrates a manufacturing processing space where multiple deformation histories target a similar final geometry. For example, by applying asymmetrical deformations by a single tool in SPIF versus constrained squeezing deformations of two tools in DSIF [8–11]. These distinct deformation histories can lead to differing local properties and microstructures, which ultimately can be associated with global behaviors through multiscale modeling techniques.

Typical length scales of interest in metal forming include microscale lengths scales capturing behavior of polycrystalline grain structures and macroscopic length scales capturing loads imposed by the manufacturing process [2, 3]. Crystal plasticity (CP) models are capable of capturing the grain-scale response by tracking the deformation of individual grains in a representative polycrystal volume [12–14]. Therefore, CP models allow characterization of the anisotropic behavior and evolution of crystallographic texture resulting from significant plastic deformation during forming processes. A multiscale CP finite element (FE) simulation incorporates microscale CP methods into a large-strain FE simulation at which macroscale boundary conditions are applied. This may be done using *hierarchical* methods where models are run independently at different length scales and information is passed between them, or *concurrent* methods where the models are run at the same time.

Hierarchical methods have been utilized in metal forming research by using CP models to fit anisotropic constitutive laws (such as Hill [15], Cazacu et al. [16]) to capture macroscale mechanical behavior and crystallographic texture [3]. Esmaeilpour et al. [17] applied this approach to incremental forming of aluminum sheets using the Yld2004–18P yield function and showed good agreement of forming force results with experiments [18]. For texture prediction, Mishra et al. [19] used SPIF FE results as inputs into a mean-field CP solver (VPSC [20]) and evaluated the resultant texture at particular material points. Rakshit et al. [21] developed a coupled macroscale FE-CP simulation framework for SPIF in Al-Li alloys which used experimental data to concurrently fit both a VPSC CP model and macroscale Hill48 model, and then correlated macroscale SPIF FE and microscale CP results.

While proven effective in some cases, hierarchical methods require considerable effort and expertise to decide on appropriate macroscale models to use in order to capture relevant anisotropic information, and limitations of when the true multiscale behavior may deviate from the fitted response. Concurrent methods can offer more accurate representations of multiscale responses, as the information is directly evaluated “on-the-fly" instead of being passed and fit between the multiple models. These models, also known as *embedded* models, have been applied to metals by embedding FFT-based CP or mean-field CP models into FE frameworks [22] and demonstrated for both implicit [23] and explicit [24, 25] methods. However, concurrent methods are typically slow and expensive due to the number of state variables necessary for orientation and hardening of each grain [23] and therefore limiting for forming applications.

More recently, machine learning (ML) surrogate models have been used in place of expensive microscale models to significantly accelerate concurrent multiscale methods [26]. In particular, recurrent neural networks (RNNs) have been used by various researchers to model history-dependent phenomena such as path-dependent plasticity. For example, Mozaffar et al. [27] used RNNs to predict stress in plasticity models of nonlinear composites, and Gorji et al. [28] used RNNs to predict stress of an anisotropic plasticity model given arbitrary loading paths. Logarzo et al. [29] used RNNs to model a homogenized inelastic microstructure with soft inclusions and incorporated the response into a macroscale implicit FE framework. But, the use of RNN surrogate models in explicit FE frameworks requires additional considerations. Explicit FE analyses typically feature many small timesteps due to conditionally stable time increments and it is accordingly infeasible to generate training data at that resolution. Therefore, the concept of self-consistency, or, that learned stress history is independent of strain-path discretization, is particularly important. Bonatti and Mohr [30] have developed a RNN-based formulation called Linear Minimal State Cells (later used in this work) which mathematically enforce self-consistency. Liu et al. [31] also developed a continuous recurrent neural operator to address the issue of self-consistency and applied this to explicit FE.

Surrogate modeling methods have additionally been demonstrated for CP constitutive responses [31, 32] and texture evolution [33–35]. Yuan et al. [33] used a reduced-order representation of texture using principal component analysis of spherical harmonic coefficients and a random forest algorithm to learn final texture given an initial texture and strain path. Ali et al. [34] used an artificial neural net (ANN) to predict texture and stress response of polycrystals of AA6063-T6. Ibragimova et al. [35] similarly used an ANN to predict stress and texture of FCC materials under arbitrary non-monotonic loading paths. These methods are ready to be extended to microstructural evaluation in manufacturing load cases, as we demonstrate in this work.

In this work, we use ML surrogate models to develop efficient workflows and multiscale models that capture full-field microstructural behavior in single-point incremental forming. The work is organized as follows. Section Simulation Framework develops the basis of the multiscale model

through a crystal plasticity model and macroscale SPIF finite element framework. Section Multiscale Methodology then details two generalized multiscale workflows using ML surrogate models for constitutive response and texture evolution. We show accurate approximations using all ML surrogate models through appropriate dataset generation, training, and validation. This includes prediction of texture evolution enabled by reduced order representation. These multiscale workflows are then applied to manufacturing applications of SPIF in Section Multiscale Workflow Results. We show good agreement between workflow results for macroscale forming parameters and texture for two unique tool paths, and demonstrate reduced computational cost for multiscale models and full-field texture prediction. Section Discussion then provides a discussion on the work, and Section Conclusions presents the conclusions.

Simulation Framework

Multiscale CP simulations were performed using macroscale FE analysis and evaluation of a microscale CP response at each material point. On the macroscale, FE analysis was performed using ABAQUS/Explicit with boundary conditions from a SPIF process. On the microscale, the material constitutive response was defined by a visco-plastic self-consistent (VPSC) CP model. Since VPSC captures only the plastic deformation response, a Newton–Raphson (NR) iteration scheme was developed to compute the elastic–plastic response. This section describes the separate modeling approaches for each length scale.

Crystal Plasticity Model

The Visco-Plastic Self-Consistent approach (VPSC, version 8 [20]) was chosen for polycrystal plasticity modeling due to low computational cost and demonstrated effectiveness in various crystal systems. VPSC8 is a mean-field solver that approximates each single crystal grain as an ellipsoidal visco-plastic inclusion in an effective homogenized visco-plastic medium. This permits each grain to deform individually and allows for capture of texture evolution of the polycrystal and the resultant anisotropic mechanical responses. Detailed discussion on the VPSC approach can be found in Tomé and Lebensohn [20] with open-source codes available for download.

In this model, the visco-plastic constitutive behavior of a single crystal material point in the polycrystal is given through the strain-rate tensor $\dot{\varepsilon}_{ij}$,

$$\dot{\varepsilon}_{ij} = \dot{\gamma}_o \sum_s m_{ij}^s \left(\frac{|\boldsymbol{m}^s : \boldsymbol{\sigma}'|}{\tau_{CRSS}^s} \right)^n \times \text{sign}\left(\boldsymbol{m}^s : \boldsymbol{\sigma}'\right) \tag{1}$$

with reference shear strain rate, $\dot{\gamma}_o$, critical resolved shear stress, τ_{CRSS}^s, Schmidt tensor, m_{ij}^s, deviatoric stress tensor, σ'_{ij}, and microscopic rate-sensitivity parameter, n, for a given slip system, (s). The constitutive response at each material point (grain) was defined by the critical resolved shear stress using the extended Voce hardening law,

$$\tau_{CRSS}^s = \tau_0^s + \left(\tau_1^s + \theta_1^s \Gamma\right)\left(1 - \exp\left(-\Gamma \left|\frac{\theta_0^s}{\tau_1^s}\right|\right)\right) \tag{2}$$

with accumulated shear strain in the grain, $\Gamma = \Sigma_s |\gamma^s|$, initial threshold stress, τ_0^s, initial hardening rate, θ_0^s, asymptotic hardening rate, θ_1^s, and back-extrapolated flow stress, $(\tau_0^s + \tau_1^s)$.

The VPSC model was run using an n-effective linearization interaction parameter, $n^{eff} = 10$, which provides a response in-between a stiff Taylor-bound approximation of uniform strain-rate in all grains and a compliant Sachs-bound approximation of uniform stress in all grains. A rate-insensitive formulation was used which scales $\dot{\gamma}_o$ to the norm of the macroscopic strain rate. This has the effect of enforcing rate-insensitivity when τ_{CRSS}^s is not a function of rate, as is the case with the extended Voce law, and when n is sufficiently large (≥ 20) [36].

An Al5052-H32 material system was chosen due to being a common material in forming applications. A random input texture with 500 grains was generated using MTEX 5.10.2 [37] and parameters for the extended Voce hardening law were taken from experimentally measured values in Chen et al. [38] with $\tau_0^s = 65$ MPa, $\tau_1^s = 9$ MPa $\theta_0^s = 55$ MPa, and $\theta_1^s = 23$ MPa, with a VPSC rate-sensitivity parameter, $n = 20$.

Newton–Raphson Iteration Scheme

A Newton–Raphson iteration scheme was used to implement an elastic–plastic response using generalized Hooke's law for an isotropic elastic solid and the defined VPSC model. Elastic constants were assumed constant throughout the analysis using common values for aluminum of $E = 70$ GPa for Young's modulus and $\nu = 0.33$ for Poisson's ratio. This assumption of constant values was validated by inputting strain paths from SPIF results (in Sect. Texture) into the base VPSC model. It was observed that all elastic constants showed a limited change ($< 0.8\%$) over the full simulation time history for highly strained elements.

The NR framework was developed by considering additive decomposition of the total strain into elastic and plastic components, $\varepsilon = \varepsilon_e + \varepsilon_p$ and the stress response at subsequent timestep $\sigma_{t+\Delta t}$ using generalized Hooke's Law:

$$\sigma_{t+\Delta t} = \sigma_t + C : \left(\Delta\varepsilon - \Delta\varepsilon_p\right) \tag{3}$$

where C is the elastic stiffness tensor, and stress, σ, and strain, ε, quantities were defined in Voigt notation as 6x1 vectors. Yield was checked at each increment to determine if an elastic or plastic update was performed. A value of $\sigma =$ 160 MPa was chosen as the threshold for a plastic update. This check was used to improve computation speed of the algorithm and avoid unnecessary convergence iterations in the elastic regime. Plastic updates did not force nonlinear (inelastic) behavior and the algorithm was able to converge even with plastic strain increments close to zero, however, this was more expensive than applying updates using the elastic relation.

During a plastic update, the deviatoric components of the stress response were assumed to be dominated by the plastic response due to the high plastic strains experienced during forming processes. This permitted stress to be written as a function of VPSC through decomposition into deviatoric, σ', and hydrostatic, σ^h, components, corresponding, respectively, to the plastic VPSC response, and product of the bulk modulus, K and volumetric strain, ε_v.

$$\sigma_{t+\Delta t} = \sigma'_{t+\Delta t} + \sigma^h_{t+\Delta t} = \text{VPSC}\left(\Delta\varepsilon_p\right) + \sigma^h_t + K * \Delta\varepsilon_v \tag{4}$$

where $\Delta\varepsilon_v$ in the incremental volumetric strain. VPSC8 allows inputs as variable velocity gradient histories, which can be expressed by appropriate plastic strain increment ($\Delta\varepsilon_p$) histories with equal time durations under rate-insensitive conditions. The NR iteration scheme was formulated by minimizing residual function, f, between Eqns. (3) and (4)

$$f\left(\Delta\varepsilon_p\right) = 0 = C : \left(\Delta\varepsilon - \Delta\varepsilon_p\right) - \text{VPSC}\left(\Delta\varepsilon_p\right) - K * \Delta\varepsilon_v + \sigma'_t \tag{5}$$

and solving for plastic strain increment $\Delta\varepsilon_p$,

$$\Delta\varepsilon_{p_{k+1}} = \Delta\varepsilon_{p_k} - J_f\left(\Delta\varepsilon_{p_k}\right)^{-1} * f\left(\Delta\varepsilon_{p_k}\right) * \alpha \tag{6}$$

where $\Delta\varepsilon_{p_{k+1}}$ and $\Delta\varepsilon_{p_k}$ are the plastic strain increment at the next and current NR increment, respectively; α is a numerical damping factor, and J_f is the computed Jacobian of the residual function,

$$J_f = \frac{\partial\left[f\left(\Delta\varepsilon_p\right)\right]}{\partial\left(\Delta\varepsilon_p\right)} = -\left(\frac{\partial\left[\text{VPSC}\left(\Delta\varepsilon_p\right)\right]}{\partial\left(\Delta\varepsilon_p\right)} + C\right) \tag{7}$$

Computation of J_f required calculation of the derivative of the VPSC model which was found numerically using a three-point central difference method and resulted in a 6x6 tensor:

$$\frac{\partial\left[\text{VPSC}\left(\Delta\varepsilon_{p,i}\right)\right]}{\partial\left(\Delta\varepsilon_{p,j}\right)} = \frac{\text{VPSC}\left(\Delta\varepsilon_{p,i} + \delta\varepsilon_{p,j}\right) - \text{VPSC}\left(\Delta\varepsilon_{p,i} - \delta\varepsilon_{p,j}\right)}{2\delta\varepsilon_{p,j}} \tag{8}$$

where $\delta\varepsilon_p$ is the strain increment used to compute the derivative. This value was chosen as 0.002 which produced the most stable convergence behavior. After convergence was attained, the resulting plastic strain increment was input back into Eqn. (3) to find the total stress value.

The NR approach may not always converge depending upon initial starting point or poor calculation of the Jacobian [39]. Due to the representation of VPSC using surrogate models in the final multiscale framework, numerical methods used for derivative calculation created challenges with noisy gradient calculations and therefore required a modified damped form of the NR method to improve convergence properties.

A modified damped NR algorithm with initial value of $\alpha = 0.01$ and a single Jacobian calculation at the beginning of the analysis was used for 1000 iterations. After 1000 iterations, an Adaptive Moment Estimation (Adam) [40] algorithm was used if convergence was not obtained. The convergence criterion was defined as when the magnitude of all residual components was below 1 MPa. Oscillatory behavior of residuals was checked every 25 NR iterations and α was decreased by a factor of 0.25 if observed. The following Adam parameters were used: $\beta_1 = 0.9$, $\beta_2 = 0.999$, $\alpha_{adam} =$ 1e-6, $\epsilon_{adam} =$ 1e-7. Finally, if the number of iterations exceeded 6000, the best value was taken from all prior iterations and the analysis proceeded to the next increment.

Finite Element Modeling of Single-Point Incremental Forming

FE simulations were performed using ABAQUS/Explicit under quasi-static assumptions. Explicit FE analysis was chosen due to the lower computational cost of explicit methods than implicit methods for highly nonlinear behavior typical in forming simulations, such as changing contact definitions, material nonlinearity, and large deformations.

Figure 1a shows a schematic of the FE framework. Displacement boundary conditions were applied to a discrete rigid tool which contacted and deformed the workpiece into a final geometry by tracing a spiral tool path. The initial workpiece geometry was a 150 x 150 x 1 mm plate with fully fixed edges, and was modeled with 10,000 C3D8R reduced-order hexahedral elements with enhanced hourglass control.

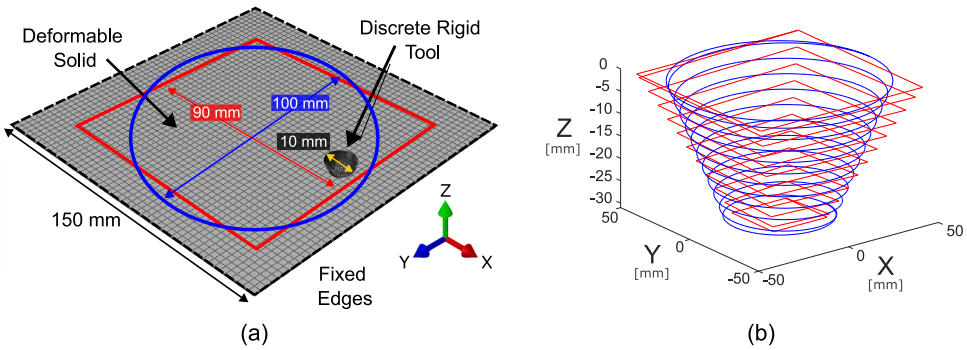

Fig. 1 Single-point incremental forming finite element analysis (**a**) schematic and (**b**) tool paths for truncated pyramid and cone tool paths

4 elements through the thickness were used (2.5 x 2.5 x 0.25mm mesh size) in order to capture through-thickness shear strains. The tool geometry was a 10 mm diameter hemisphere, and was modeled with 5808 R3D4 rigid linear quadrilateral elements.

Surface-to-surface contact was defined using a frictional coefficient of 0.15 between the workpiece and tool. The tool surface was defined as the main (workpiece as the secondary) contact surface and forming forces were extracted as reaction forces on the rigid tool. A finer mesh on the rigid tool was used to improve resolution of contact forces. Mesh sizing of the workpiece was chosen to capture localized behavior, minimize artificial strain energy, and limit computational cost. Artificial strain energy was observed to remain below 13.5% of the internal energy for all simulations. This value was validated through comparison of elastic–plastic simulations of the toolpaths using incompatible mode elements, which exhibited no artificial strain energy. Plastic strains, elastic strain energy, and forming forces showed good agreement between reduced-order and incompatible mode elements which confirmed validity of this artificial strain energy ratio for the simulation framework.

Time and mass scaling were also performed to decrease computational cost of the simulations which had an average of 800,000 timesteps. The velocity of the tool was set to 3 m/s and mass scaling was applied once at the start of the simulation to limit initial timestep to 2e-6 s. Kinetic energy was observed to remain under 5% of the internal energy for all simulations after initial deformation passes which validated the quasi-static assumptions. This tool velocity and kinetic energy ratio are comparable to those in other studies [8], which showed negligible effects through comparison to experiments.

A 45 degree truncated pyramid and 45 degree truncated cone tool path were created in MATLAB and are shown in Fig. 1b. Both tool paths included an initial small pass at a constant depth, forming path, final pass at a constant depth, and removal of tool. The cone diameter was chosen as 100 mm and pyramid base was chosen as 90 mm to match overall forming path length (3 m) between both geometries. An initial small pass of 1 mm depth was chosen to help minimize kinetic energy by avoiding large deformations during early timesteps of the simulation. Subsequent cone and pyramid tool paths then followed with linearly decreasing depths up to 31 mm with step depth around 3 mm per full revolution for a total of 10 passes.

The total depth was chosen to match similar values demonstrated in literature for SPIF of Al5052 alloys with truncated pyramid and truncated cone toolpaths [41, 42]. The step depth and number of passes were correspondingly chosen to minimize computational cost (i.e., maximize step depth, minimize passes) while keeping step depth comparable to relevant literature values, which have been demonstrated up to 3 mm in Al7075-O alloys [9]. Increasing step depth showed expected sharp step-like responses in strain histories of local material points. Although step depth has been shown experimentally to influence formability [43], the constitutive behavior of this study does not include failure and damage, and therefore this value does not affect numerical results or workflow validation.

Multiscale Methodology

Three ML surrogate models for CP were developed in this work to capture the constitutive behavior and texture evolution:

1. ML-VPSC, a surrogate model for the crystal plastic constitutive behavior
2. ML-EVPSC (elastic-VPSC), a surrogate model for the deviatoric elastic-crystal plastic constitutive behavior
3. ML-Tex (texture), a surrogate model for texture evolution

Two multiscale modeling workflows were then developed utilizing these ML surrogate models.

1. MS-NR (multiscale Newton–Raphson), a multiscale workflow which computes the elastic–plastic response

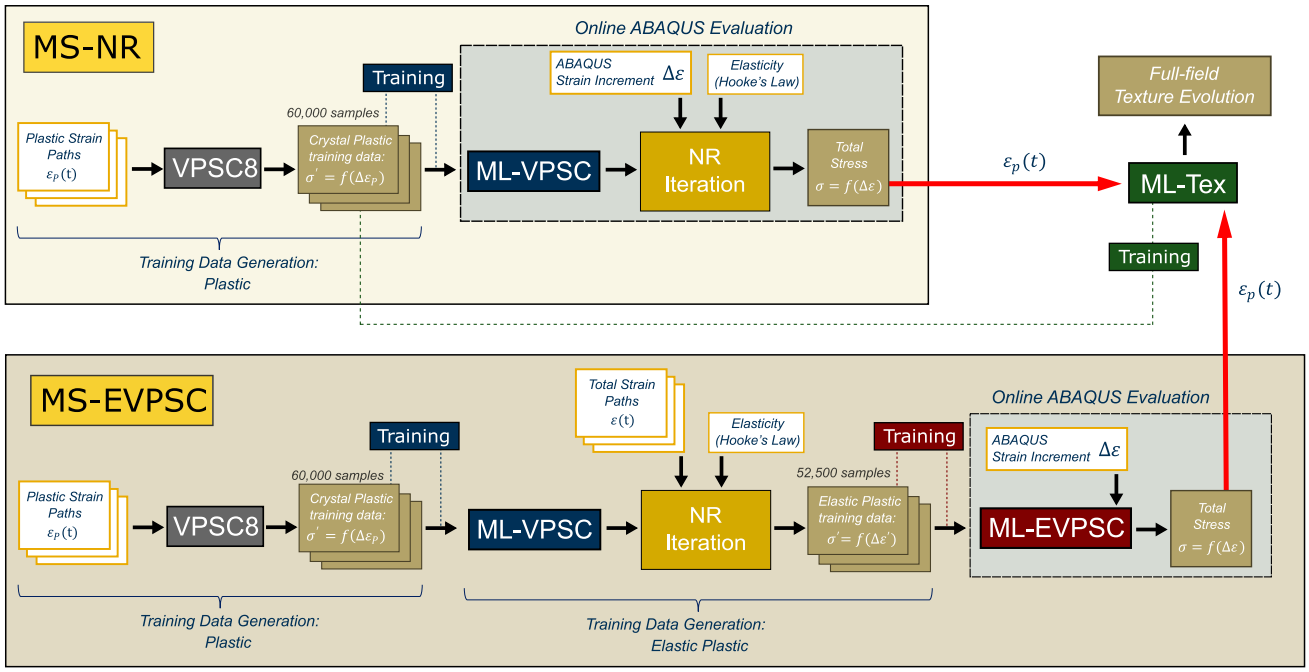

Fig. 2 Diagram showing process for model generation and evaluation of MS-NR and MS-EVPSC multiscale workflows

using ML-VPSC and the NR iteration scheme described in Sect. Newton–Raphson Iteration Scheme

2. MS-EVPSC (multiscale elastic-VPSC), a multiscale workflow which computes the elastic–plastic response using ML-EVPSC

Both multiscale workflows followed the general path of: create surrogate model training data, train the ML surrogate, use the ML surrogate in a macroscale ABAQUS simulation, and use plastic strain history results to evaluate texture evolution through ML-Tex. Figure 2 shows a schematic of these workflows. Both multiscale workflows model the same behavior. MS-EVPSC was developed to decrease the cost of the online ABAQUS simulation. This is realized by the cost of NR iterations in MS-NR being 'pre-computed' by creating an additional elastic–plastic training data set and surrogate model, and therefore excluded from the online portion of the ABAQUS evaluation of MS-EVPSC.

Surrogate Modeling of Constitutive Behavior

Surrogate models were developed for the plastic (ML-VPSC) and elastic–plastic (ML-EVPSC) constitutive behavior using data generated by the VPSC CP model and NR iteration scheme. This section describes the generation of the datasets, distributions of the input and output features, and training and validation of the ML surrogate models.

Dataset Generation

Training data for both plastic and elastic–plastic constitutive behavior consisted of input strain increment histories and output deviatoric stress histories. Plastic strain increment–deviatoric stress results produced using the base VPSC model were used for plastic training data, and deviatoric strain increment–deviatoric stress results produced using the NR iteration scheme were used for elastic–plastic training data.

Figure 3a shows example strain component paths for a single ML-VPSC sample. Strain paths were generated using a Gaussian process regression (GPR) model [44] to create smoothly varying paths with 150 timesteps for each tensorial strain component. Kernel hyperparameters were initialized with a variance of 1 and length scale of 1, with the length scale constrained to bounds of 10e-8 to 10e2. Four equidistant points along the path were used as data points for fitting the GPR model. The output (strain) value at each point was randomly selected between strain bounds, and sequentially scaled by factors of 0.25, 0.5, 0.75, and 1, to create a ramped profile. Gaussian noise with a mean of 0 and standard deviation of 0.001 was then added to the strain paths.

The strain paths were converted into strain increment paths, shown in Fig. 3b, which were input to the base VPSC model. Recall that VPSC8 allows inputs as variable velocity gradient histories which can be represented by strain

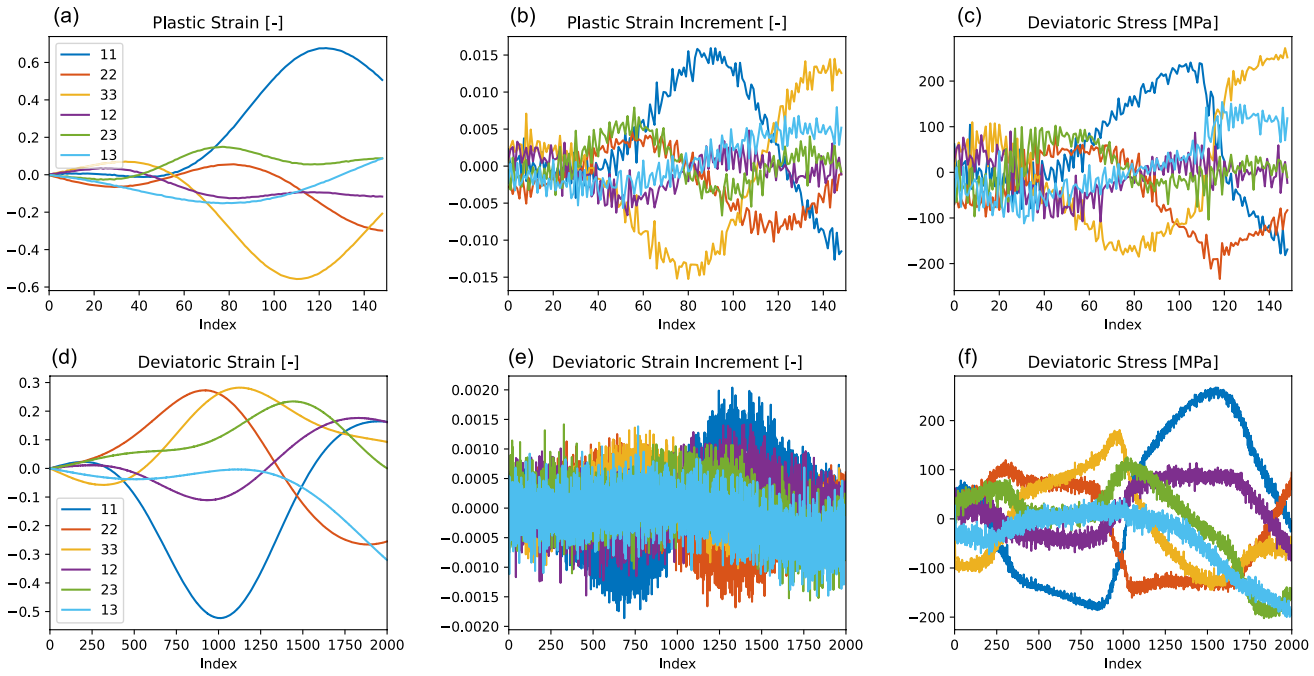

Fig. 3 Training data sample strain histories, strain increment histories, and deviatoric stress histories for ML-VPSC (**a**), (**b**), (**c**), and ML-EVPSC (**d**), (**e**), (**f**), respectively

increment histories with equal time durations under rate-insensitive conditions. VPSC output the deviatoric stress for the given inputs, shown in Fig. 3c.

Elastic–plastic training data paths were generated in a similar manner using a GPR model, but with 2000 timesteps. Figures 3d and 3e show the corresponding strain paths and strain increments. Output deviatoric stress results were computed using the NR iteration scheme and shown in in Fig. 3f. In this scheme, ML-VPSC was used in lieu of the base VPSC model. This required training of the ML-VPSC model before the ML-EVPSC dataset could be generated, but offered computational speedup. The average cost of a 150 timestep VPSC simulation was about 50 s (3.0 timesteps/sec) and the average cost of a 2000 timestep NR simulation was about 120 s (16.67 timesteps/sec). We note the high noise in the ML-EVPSC dataset also necessitated use of the Adam algorithm of the NR iteration scheme to improve convergence and allow dataset generation.

Table 1 shows the datasets of this work including number of samples, strain bounds, and noise levels. Samples were split evenly between noisy and smooth data. Figure 4 shows the histograms of this data with total strains, strain increments, and deviatoric stress components outputs of the plastic training data (Figs. 4a-c) and elastic–plastic training data (Figs. 4d-f).

60,000 total samples of 150 timesteps with 6 strain components were generated for the ML-VPSC training dataset. Strain paths were generated to reflect deformation histories common to those in incremental forming such as increasing strain values defined as a 'ramp' and plane strain conditions with thinning along the sheet thickness with maximum axial strain values of ±85% and maximum shear strain values of

Table 1 Summary of training datasets for plastic (P) and elastic–plastic (EP) constitutive behavior

P/EP	Data	Samples	ε_{11}	ε_{22}	ε_{33}	ε_{12}	ε_{23}	ε_{13}	ε_{noise}
P	Ramp	40,000	−0.85-+0.85	−0.85-+0.85	−0.85-+0.85	−0.35-+0.35	−0.35-+0.35	−0.35-+0.35	0, ±0.001
P	Plane Strain–ε_{11}	10,000	−0.10-+0.85	0	−0.85-+0.10	0	0	0	0, ±0.001
P	Plane Strain–ε_{22}	10,000	0	−0.10-+0.85	−0.85-+0.10	0	0	0	0, ±0.001
EP	Ramp	30,000	−0.85-+0.85	−0.85-+0.85	−0.85-+0.85	−0.35-+0.35	−0.35-+0.35	−0.35-+0.35	0, ±0.00010, ±0.00025
EP	Low Axial	7,500	0	0	0	−0.35-+0.35	−0.35-+0.35	−0.35-+0.35	0, ±0.00010, ±0.00025
EP	Low Shear	7,500	−0.85-+0.85	−0.85-+0.85	−0.85-+0.85	0	0	0	0, ±0.00010, ±0.00025
EP	Low Strain	7,500	−0.01-+0.01	−0.01-+0.01	−0.01-+0.01	−0.01-+0.01	−0.01-+0.01	−0.01-+0.01	0, ±0.00010, ±0.00025

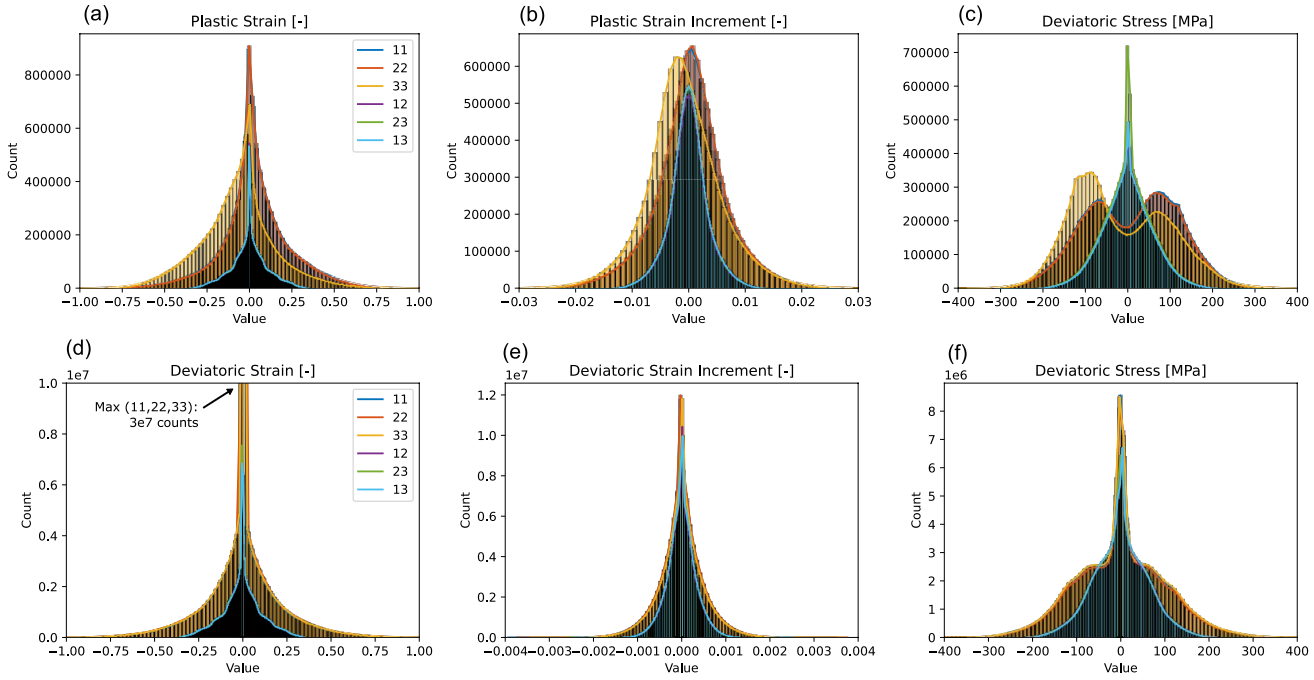

Fig. 4 Histograms of training datasets for ML-VPSC (plastic behavior) of (**a**) plastic strains, (**b**) plastic strain increments, (**c**) deviatoric stresses; and ML-EVPSC (elastic–plastic behavior) of (**d**) deviatoric strains, (**e**) deviatoric strain increments, and (**f**) deviatoric stresses

±35%. 'Ramp' samples were also used as the data set for texture evolution (ML-Tex) described in Sect. Surrogate Modeling of Texture Evolution. 52,500 total samples of 2000 timesteps with 6 strain components were generated for the ML-EVPSC training dataset with 'ramp', low axial, low shear, and low total strain features. The number of increments and noise levels were chosen to represent values observed in explicit simulations of SPIF, and data with low axial, low shear, and low total strains were generated to facilitate learning of the elastic response.

Linearized Minimal State Cells

Traditional recurrent neural networks such as long short-term memory and gated recurrent unit networks show dependence on training increment size [30]. This leads to worse performance when evaluated at different discretizations than that of training (where discretizations refers to number of timesteps in each sample) which presents challenges for explicit FEA. Explicit analyses in this work have more than 800,000 timesteps and it is not computationally feasible to generate training data of this length. Therefore, special consideration must be taken for surrogate modeling of the constitutive response for implementation into an explicit FE model.

We use a custom formulation of a RNN developed by Bonatti and Mohr [30] for surrogate modeling of the plastic and elastic–plastic response called a Linearized Minimal State Cell (LMSC). This formulation defines a transition function of the RNN which satisfies a mathematical form of self-consistency (or, invariance toward timestep-discretization) when considering a path of strain increments. For example, a strain path of 150 timesteps may be re-discretized into smaller increments of 1500 timesteps to attain the same final strain state. For a rate-insensitive quasi-static loading case, these discretizations will produce the same stress response. Ultimately, LMSCs permits training of surrogate models at computationally feasible resolutions and accurate evaluation of the models at a higher (finer) resolutions.

Training and Validation: ML-VPSC

ML-VPSC was trained on the plastic data compiled in Table 1. Inputs to the model were arrays of plastic strain increment components and outputs were arrays of deviatoric stress components. Output values were standardized by a constant value, $\sigma_0 = 85$ MPa, to target an average standard deviation of 1 for all features. Dimensionality of the inputs and outputs were 60,000 samples x 150 timesteps x 6 features. (i.e. $\sigma_{11}, \sigma_{22}, \sigma_{33}, \sigma_{12}, \sigma_{13}, \sigma_{23}$).

An LMSC with 100 state variables, 3 quadratic layers with 100 neurons, and a fully connected dense layer was used for the surrogate model. The model was trained using a Intel i9–13,900 H CPU for 350 epochs with a batch size of 32, mean squared error loss function, and stepped learning

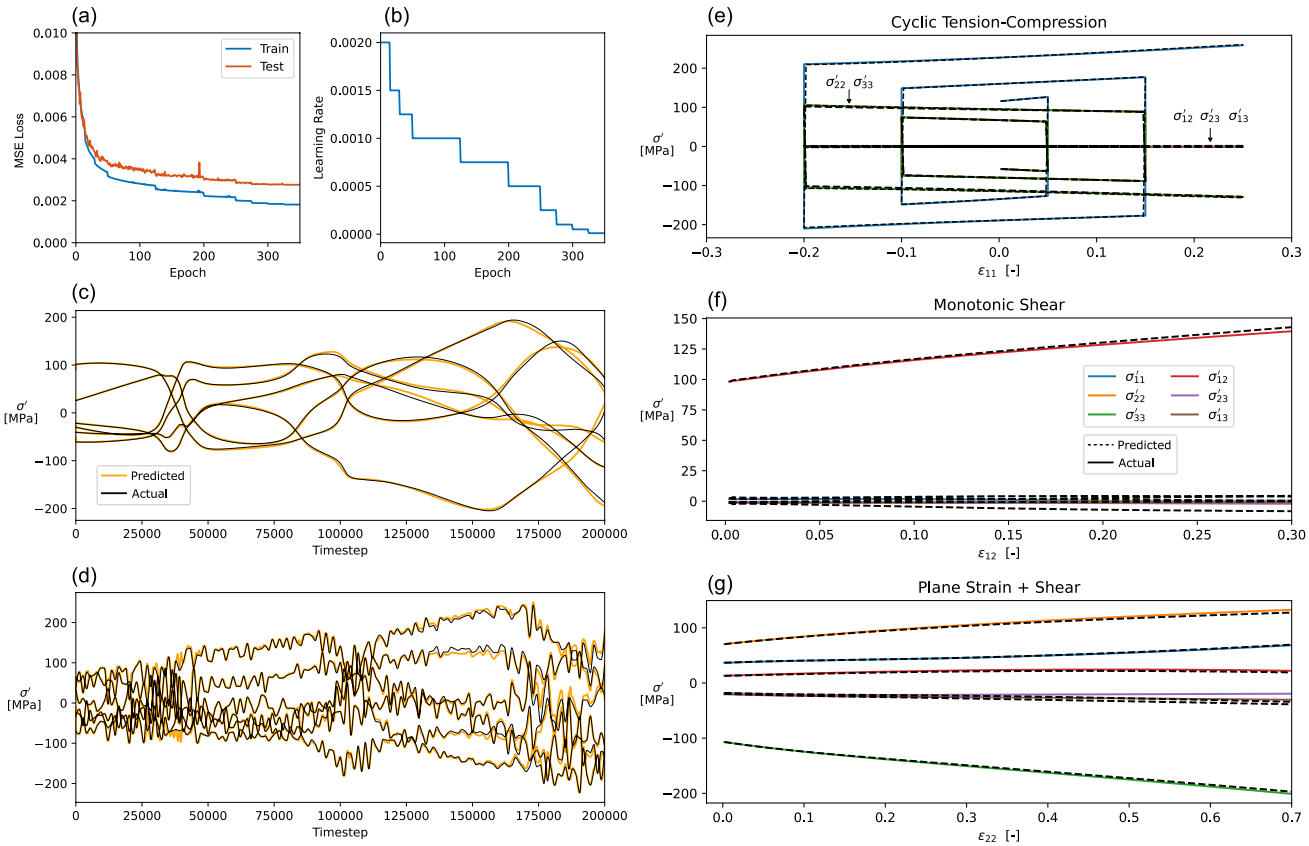

Fig. 5 Surrogate modeling results for ML-VPSC. Training: (**a**) loss history, (**b**) learning rate schedule, Testing: (**c**) re-discretized smooth path, (**d**) re-discretized noisy path, and Validation: (**e**) cyclic tension-compression, (**f**) monotonic shear, (**g**) plane strain and shear

rate schedule. A 90% training, 10% testing split was used to separate the dataset.

Figure 5a shows the testing and training loss history as a function of epochs and Fig. 5b shows the corresponding learning rate. An example of ML-VPSC predictions on a testing set sample are shown in Fig. 5c for a smooth strain path and Fig. 5d for a noisy strain path. Higher prediction accuracy at earlier timesteps was observed for both paths. Timestep-invariance is also demonstrated as the strains paths are re-sampled discretizations of 200,000 timesteps which correspond to 1,333x the original training resolution (150 timesteps).

Performance of the model was then validated against deformation paths not included in the training dataset: cyclic tension/compression in the +11 direction up to 25%, monotonic shear in the +12 direction up to 30%, and monotonic plane strain with shears: 17.5% in +11, 52.5% in +22, -70% in +33, 13.125% in +12, −13.125% in +23, and − 13.125% in +13. Figures 5e-g show the validation results of deviatoric stresses compared to ground truth data computed using VPSC, which was produced by inputting the same strain paths into both VPSC and ML-VPSC. Larger errors were observed at later timesteps, corresponding to higher strains on the plots, with the largest deviations up to 15 MPa for σ'_{23} in plane strain with shear loading conditions. Plane strain deformation histories were intentionally selected to be included in plastic training data, as these deformations are typical in forming. Performance for stress predictions of plane strain deformation paths was improved following inclusion of this data.

Training and Validation: ML-EVPSC

ML-EVPSC was trained using the elastic–plastic data compiled in Table 1. Inputs to the model were arrays of (total) deviatoric strain increment components and outputs were arrays of deviatoric stress components, with dimensionality: 52,500 samples x 2000 timesteps x 6 input/output features. Output values were standardized by the same constant value for ML-VPSC, $\sigma_0 = 85$ MPa. A similar LMSC architecture to ML-VPSC was used with 100 state variables, 3 quadratic layers with 100 neurons, and a fully connected dense layer. This model was trained using a Intel i9–13,900 H CPU for 100 epochs with a batch size of 32, mean squared error loss function, stepped learning rate schedule, and a 90/10 training/testing dataset split. The

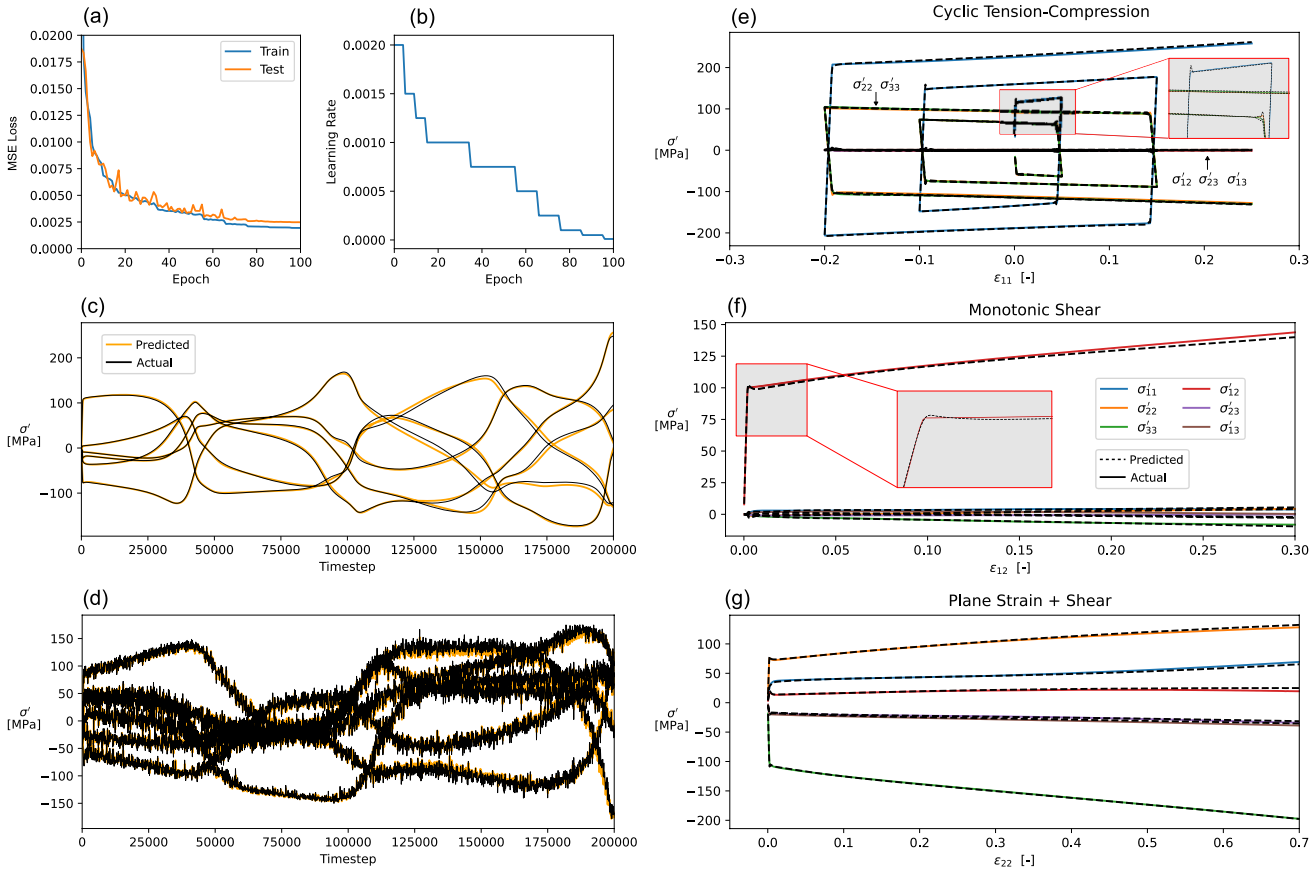

Fig. 6 Surrogate modeling results for ML-EVPSC. Training: (**a**) loss history, (**b**) learning rate schedule, Testing: (**c**) re-discretized smooth path, (**d**) re-discretized noisy path, and Validation: (**e**) cyclic tension-compression, (**f**) monotonic shear, (**g**) plane strain and shear

number of training epochs was lowered for ML-EVPSC compared to ML-VPSC as the number of input/output timesteps significantly increased the training cost.

Figure 6a shows the training and testing loss histories of the model, and Fig. 6b shows the learning rate schedule. Figures 6c and d demonstrate the performance on smooth and noisy testing samples re-discretized to 200,000 increments (100x training resolution). Figures 6e-g show validation of the ML-EVPSC model against cyclic tension/compression, monotonic shear, and plane strain with shear deformation histories (similar to those in Figs. 5e-g) computed using the NR iteration scheme and ML-VPSC. Some error was observed at the onset of plastic response which is seen as peaks of the predicted lines at the start of the nonlinear response as shown in the plot inserts in Figs. 6e and f. However, the linear (elastic) behavior up to these peaks, and nonlinear (plastic) behavior after these peaks was captured well. The largest deviation was observed again for the plane strain and shear loading at later timesteps but showed lower magnitudes of up to 4 MPa for all shear stresses.

Surrogate Modeling of Texture Evolution

A surrogate model for texture evolution, ML-Tex, was developed using plastic strain history inputs. Texture data was extracted from the same dataset for ML-VPSC generated from the base VPSC model. For each plastic 'ramp' path in Table 1, texture was output every 3 VPSC timesteps for 50 total outputs. This section discusses reduced-order representation for texture, and training and validation of ML-Tex.

Reduced-Order Representation of Texture

VPSC8 outputs texture data using 3 Euler angles for each grain. The resulting space spanned by 1500 state variables (500 grains x 3 Euler angles) required reduction to a lower-dimensional space for effective learning using ML. Reduced-order representation was performed via decomposition of the orientation distribution function (ODF) into generalized spherical harmonic (GSH) coefficients followed by principal component analysis (PCA).

Given Euler angle values, MTEX software (version 5.10.2) [37] was used to compute the ODF which can be expanded into GSH coefficients [45]. The resulting expansion terms, which we will call harmonic coefficients, allowed reduced-order representation of the texture. While the full GSH representation exists in an infinite space, it may be reduced by truncating the representative degrees. This was chosen as 16 in this work, which assuming no sample symmetry, is represented by 6454 complex coefficients. Many of these values are non-unique or zero in an FCC crystal due to symmetry, and may be further reduced to 782 values by considering only the unique values of the complex coefficients. The magnitudes of unique real values and unique imaginary values were concatenated in a 782-valued array to form the final representation.

We may compare this approach to work by Eghtesad et al. [46] who demonstrated a compact representation of a cubic system with no sample symmetry using 564 dimensions. The authors removed dimensions of negligible weight during iterative calculations and fitting of the ODF. In this work, we did not remove nonzero values and expect a larger number of dimensions for representation.

A final reduction step was performed using PCA on the 40,000 ramp strain paths with 50 textures each for a total of 2,000,000 textures. Figure 7a shows the explained variance of the principal components over the 782-dimension space defined by the unique values for the harmonic coefficients. 100 principal components (PCs) were chosen to limit dimensionality and maximize an explained variance of 94.17% for the dataset. Figure 7b shows the reconstruction of the unique harmonic coefficients when considering 100 PCs and Fig. 7c shows comparisons between the pole figures of an original and re-constructed texture. Slights differences in magnitude and sharpness of texture were observed but overall the PCA-reduced representation captured the texture information.

Training and Validation: ML-Tex

A long short-term memory (LSTM) RNN was used for the surrogate model for texture evolution, ML-Tex. As shown in the workflows in Fig. 2, texture evolution was evaluated after completion of the multiscale simulation. Therefore, generation of training data at an appropriate discretization was feasible and did not require the timestep invariance provided by LMSCs for the constitutive law surrogate models.

Inputs to ML-Tex were time histories of plastic strain components with 50 timesteps, and outputs were time

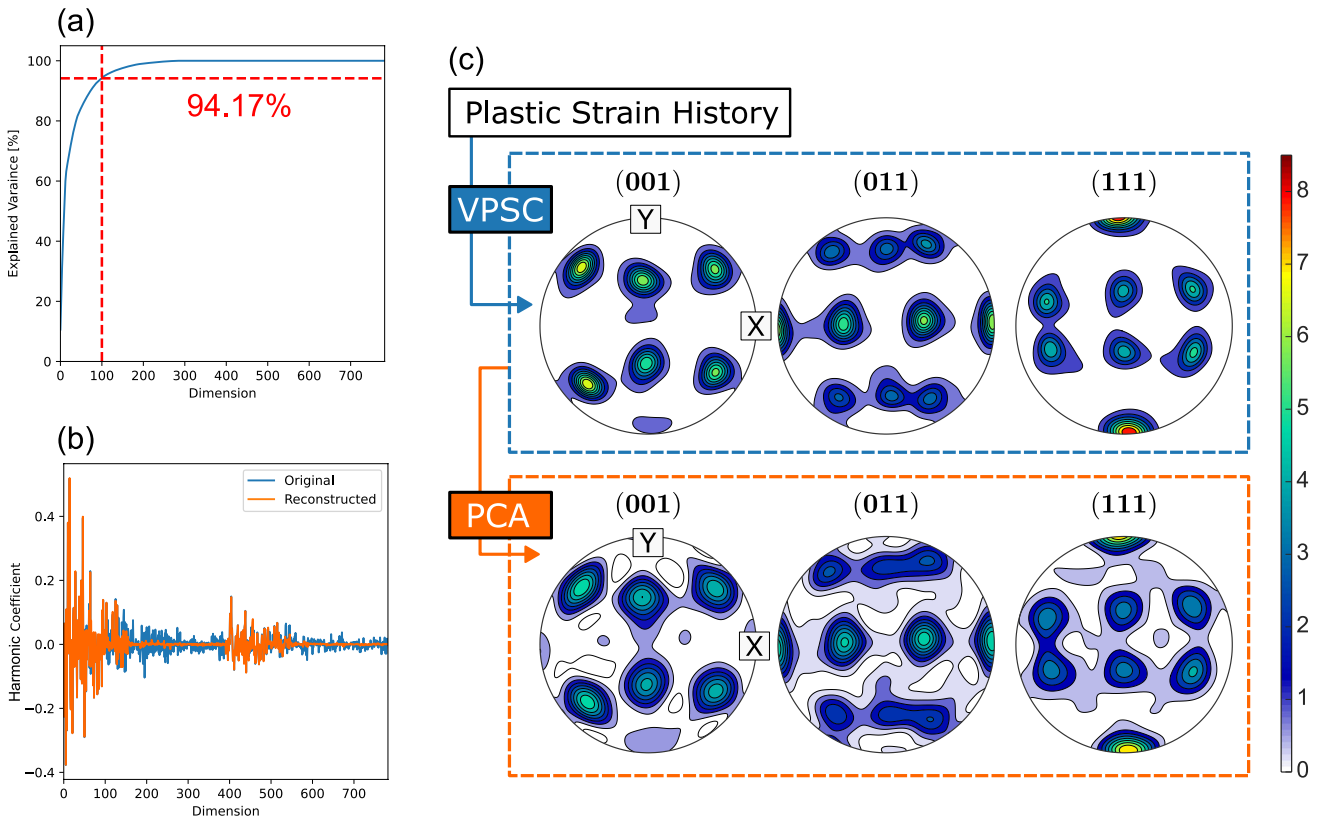

Fig. 7 Reduced order representation of texture using principal component analysis: (**a**) explained variance for principal components, (**b**) re-constructed harmonic coefficients, (**c**) comparison of baseline VPSC and PCA re-constructed texture: Scale bar represents multiples of random distribution (m.r.d)

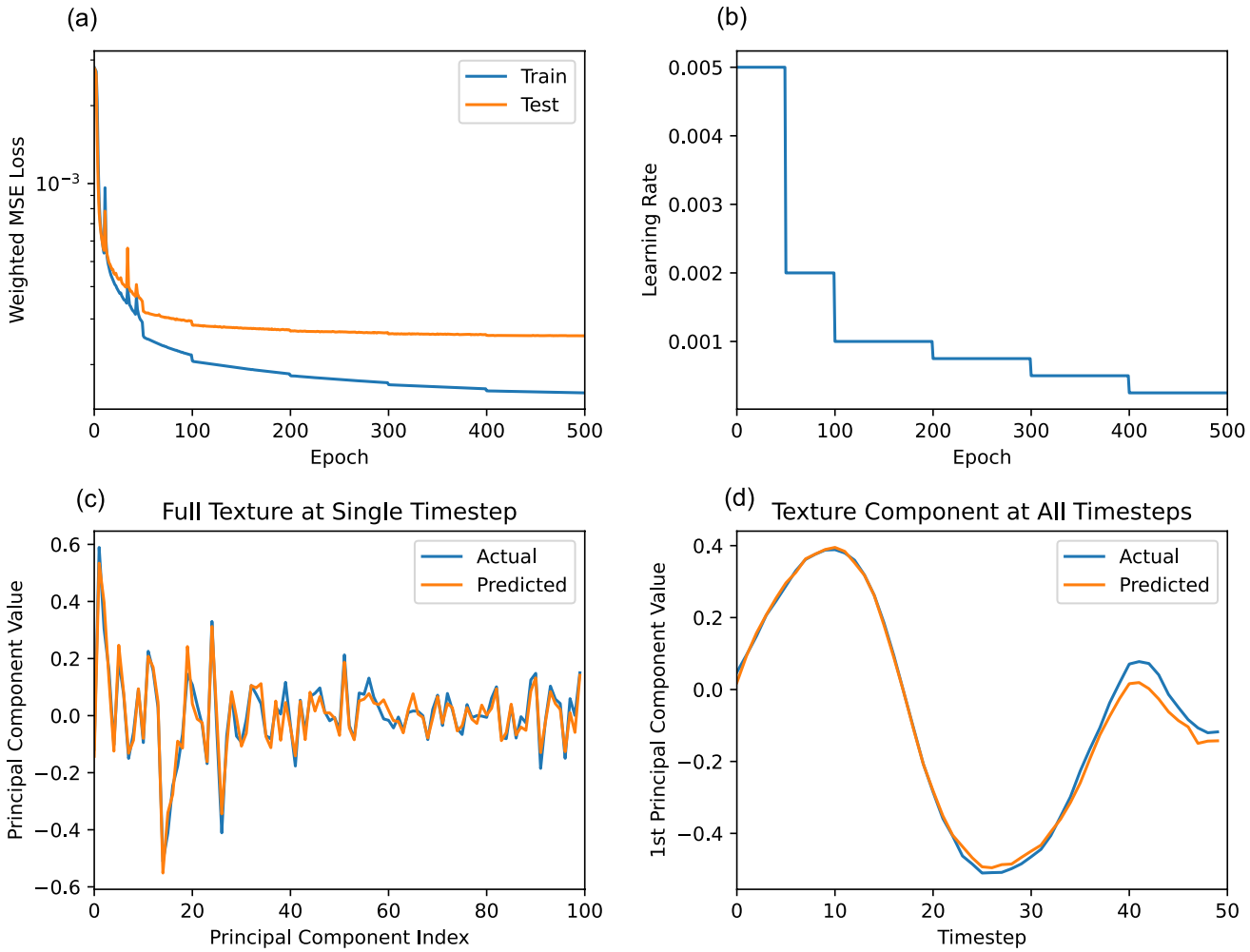

Fig. 8 Training and testing results for ML-Tex showing (**a**) loss history, (**b**) learning rate schedule, (**c**) prediction of a full texture, and (**d**) prediction of a texture component at all timesteps

histories of PCs of the reduced harmonic coefficients. The input dimensions were 40,000 samples x 50 timesteps x 6 plastic strain components and the output dimensions were 40,000 samples x 50 timesteps x 100 principal components.

An LSTM with 3 layers of 200 neurons was used with a *tanh* activation function and GPU-accelerated training using cuDNN optimized code on an NVIDIA GeForce RTX 4060 GPU. A batch size of 128 was used for 500 epochs with a stepped learning rate schedule, 80/20 training/testing dataset split, and early stopping of 75 epochs to avoid overfitting. A weighted loss function using mean squared error multiplied by explained variance for each PC was used. Figure 8a shows the training and testing loss history and Fig. 8b shows the learning rate schedule for the training process.

Figures 8c and d demonstrate prediction of a texture by comparing actual and predicted values of the PC components. The values are taken from a texture in the unseen testing set which is the same pole figure displayed in Fig. 7c. Figure 8c shows the prediction of a full texture (100 PCs) at a single timestep and Fig. 8d demonstrates prediction of a single texture component (1 PC) at all 50 timesteps throughout a strain history. Together these plots demonstrate the capability to predict full textures at multiple timesteps, or in other words, texture evolution at any material point given a plastic strain history.

ML-Tex was validated by comparing predicted textures to VPSC outputs of the validation deformation histories in Figs. 5e-g (cyclic tension/compression, monotonic shear, and plane strain with shear) as well as an additional plane strain path: up to 70% in +22 and -70% in +33. Figures 9a-d show the final textures for these strain paths using VPSC and ML-Tex. General trends are well captured among the distinct deformation paths with primary differences being magnitude of intensity values. The largest deviation appears as the magnitude difference for the monotonic +12 shear path.

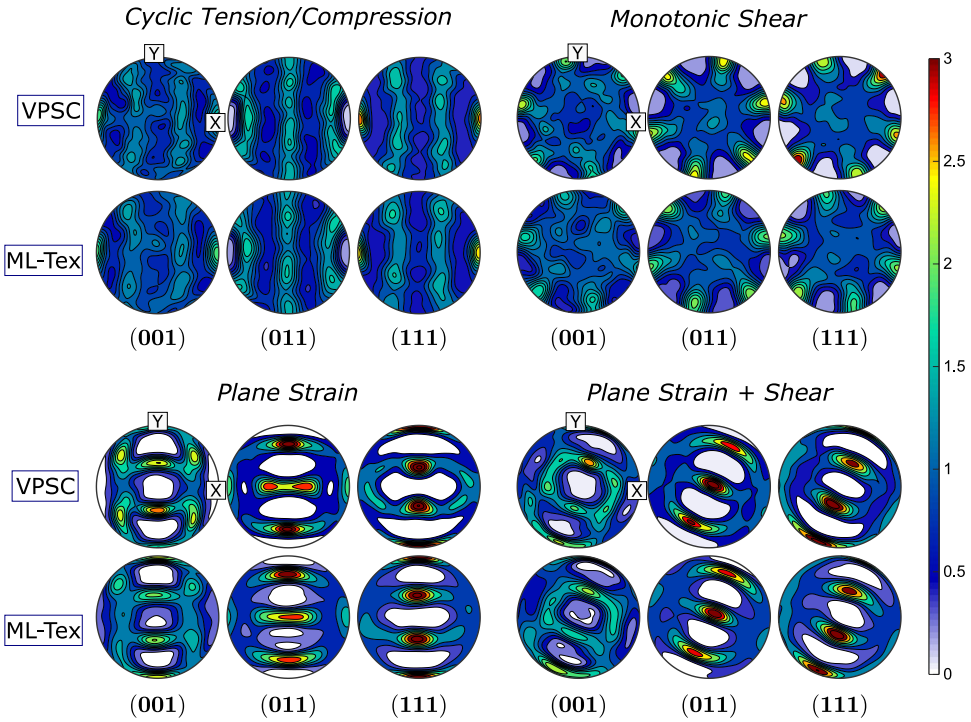

Fig. 9 Comparison of ground truth VPSC textures with predicted ML-Tex textures for various deformation histories

Multiscale Workflow Results

MS-NR and MS-EVPSC multiscale workflows were applied to FE analysis of SPIF. Results of the two multiscale models were compared using macroscopic parameters of thickness strains and forming force, and microscopic parameters of texture evolution. The implementation of the constitutive surrogate models into a Vectorized User Material (VUMAT) is discussed, followed by results for SPIF tool paths, and the computational cost of the different multiscale approaches.

Implementation of VUMAT

Surrogate models for the constitutive response (ML-VPSC, ML-EVPSC) were implemented into ABAQUS/Explicit using Vectorized User Material (VUMAT) subroutines. Two VUMATs were developed: one for ML-VPSC and one for ML-EVPSC. For each VUMAT, the weights and biases for each LMSC layer were read in and used within the LMSC architecture (architecture details found in [30]).

During the FE simulation, ABAQUS supplied a total strain increment at each timestep which was used to calculate the corresponding total stress response. The deviatoric components of each strain increment were input into the corresponding surrogate model which then computed the deviatoric stress components. The full stress response was computed by including a hydrostatic component calculated using the bulk modulus and volumetric strain increment. For the MS-NR model, a NR convergence criterion (< 1 MPa) was required to accept the current stress state, update the state variables of the LMSC, and proceed to the next step. The MS-EVPSC model did not require convergence as the elastic–plastic response was directly output. Additionally, a damping stress was included in the MS-EVPSC model to improve numerical stability which was previously explored by the authors of the model [32]. This damping stress was not included in the MS-NR model.

The output stress for the MS-NR model was computed as:

$$\sigma_{MS-NR}(t+\Delta t) = \mathrm{NR}[\Delta\hat{\epsilon}(t)] + K * \Delta\epsilon_v(t) + \sigma^h(t) \tag{9}$$

and for the MS-EVPSC model as:

$$\begin{aligned}\sigma_{MS-EVPSC}(t+\Delta t) = {} & \mathrm{ML{-}EVPSC}[\Delta\hat{\epsilon}(t)] \\ & + K * \Delta\epsilon_v(t) + \sigma^h(t) + \sigma_{damp}(t)\end{aligned} \tag{10}$$

where $\hat{\epsilon}(t)$ is the input deviatoric strain vector in Voigt notation, 'NR' is an operator representing the Newton–Raphson iteration scheme using the ML-VPSC model (Section Newton–Raphson Iteration Scheme), 'ML−EVPSC' is an operator representing the ML-EVPSC model, K is the bulk modulus, $\Delta\epsilon_v(t)$ is the incremental volumetric strain, and $\sigma_{damp}(t)$ is the numerical damping stress. The damping stress was computed as:

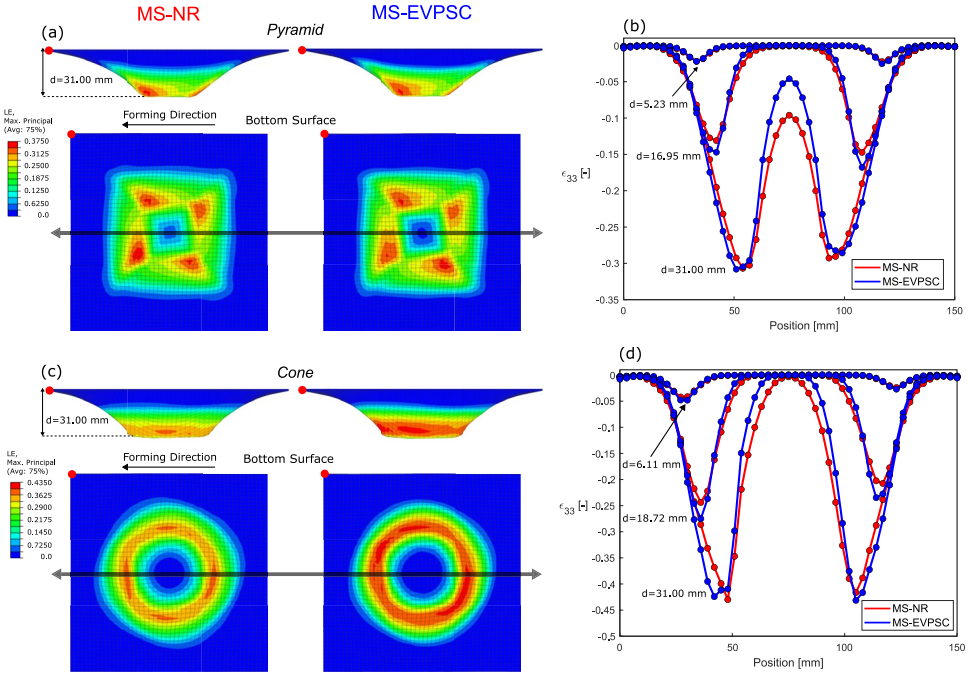

Fig. 10 Macroscopic results for logarithmic strain ε_{33} contours of (**a**) truncated pyramid and (**c**) truncated cone, and strain profiles of thinning across the workpiece at multiple forming depths for (**b**) truncated pyramid and (**d**) truncated cone

$$\sigma_{damp}(t) = \frac{\Delta\hat{\epsilon}(t)}{\|\Delta\hat{\epsilon}(t)\|} * \tanh(\nu * \|\Delta\hat{\epsilon}(t)\|/\mathrm{dt}) \tag{11}$$

where ν is a damping value set as 0.01 and dt is the ABAQUS timestep. The value of ν was chosen to be as small as possible while enabling stability within the multiscale simulation.

ABAQUS/Explicit calls the VUMAT at each time increment for a block of material points, which permits vectorization for evaluating the material response. Vectorization was not implemented for the MS-NR model because each material point experiences a unique deformation history and therefore requires different numbers of convergence iterations. However, since the MS-EVPSC model performs a single iteration per timestep, this VUMAT was fully vectorized which allowed a computational cost savings of about 10% compared to a non-vectorized form.

Single-Point Incremental Forming Results

Four multiscale simulations were carried out for: (1) a 45 degree truncated pyramid, and (2) a 45 degree truncated cone tool path using both the MS-NR and MS-EVPSC workflows.

Macroscopic Strains in Thickness

Figure 10 shows the macroscopic strain results of the simulations. Contours are shown for logarithmic strain along the plate thickness (ε_{33}) at the end of the tool path for the truncated pyramid in Fig. 10a and truncated cone in Fig. 10c. For both geometries, the MS-EVPSC models showed a larger concentration of high strains at formed corners and a larger concentration of low strains at the center of the part than the MS-NR models. Strain concentrations were also geometry dependent; both models for the truncated pyramid showed high strains at points of path direction change for each square contour.

Figures 10b and d show profiles of the ε_{33} values across the formed geometry represented by horizontal lines across the midsection of the plate in Figs. 10a and c. Each plotted point represents information at an FE integration point along the bottom surface and different lines represent strains at different forming depths, d, over the simulation. Both geometries showed strain values peak at the largest forming depth with an approximately linear decrease in strain along the wall toward low strain regions in the center and edges of the part. Low strain regions in the center region also showed the largest difference between MS-EVPSC and MS-NR values. Differences between models increased at later timesteps when larger strains were recorded, though general trends were still followed.

We note that particular modeling effort was placed on prediction of low-strain regions. It was observed that inclusion of high noise, longer timestep arrays, and inclusion of low strain data in Table 1 improved prediction of the low

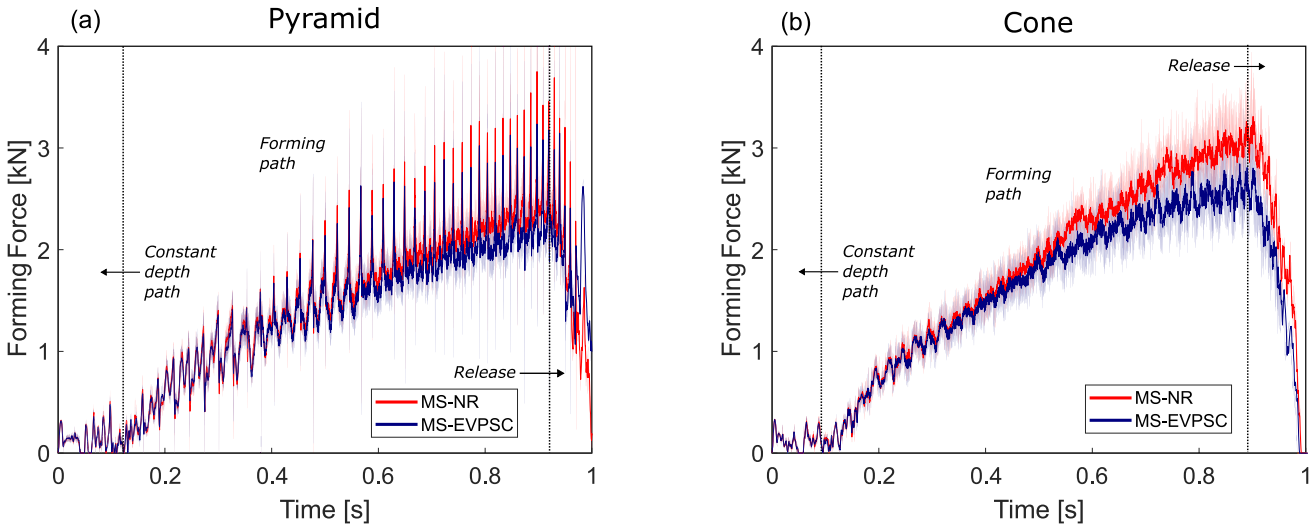

Fig. 11 Macroscopic forming force results for (**a**) truncated pyramid and (**b**) truncated cone tool paths. Low-pass filtered (thin lines) and moving-mean smoothed (thick lines) profiles are included to improve visualization

strain response in the edges and center of the formed part. Results of intermediate multiscale models during model development were used to adjust and guide appropriate training data inclusion for the surrogate models.

Forming Forces

Forming forces were extracted at every timestep from the reaction force magnitude acting on the reference point of the discrete rigid tool. Figure 11 shows the forming force results for both tool paths. For both geometries, forces were approximately constant during the initial constant depth path, increased during the forming path, and decreased as the tool was released.

Significant noise was observed in the forming force results and so a low pass filter and moving mean filter were used to post-process data. Noise decreased with higher mesh density of the discrete rigid tool and was observed to correlate with node-to-node contact with the deformable mesh workpiece. Sharp peaks in the truncated pyramid

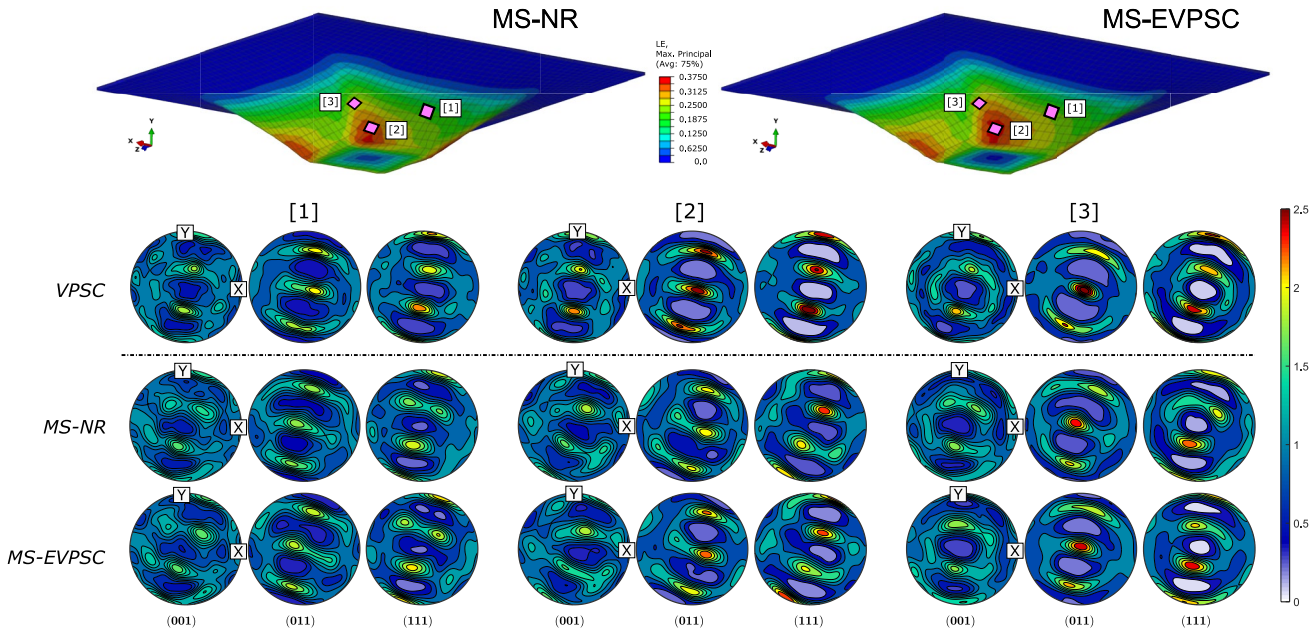

Fig. 12 Microscale texture results for truncated pyramid at various material points using the base VPSC, MS-NR, and MS-EVPSC models

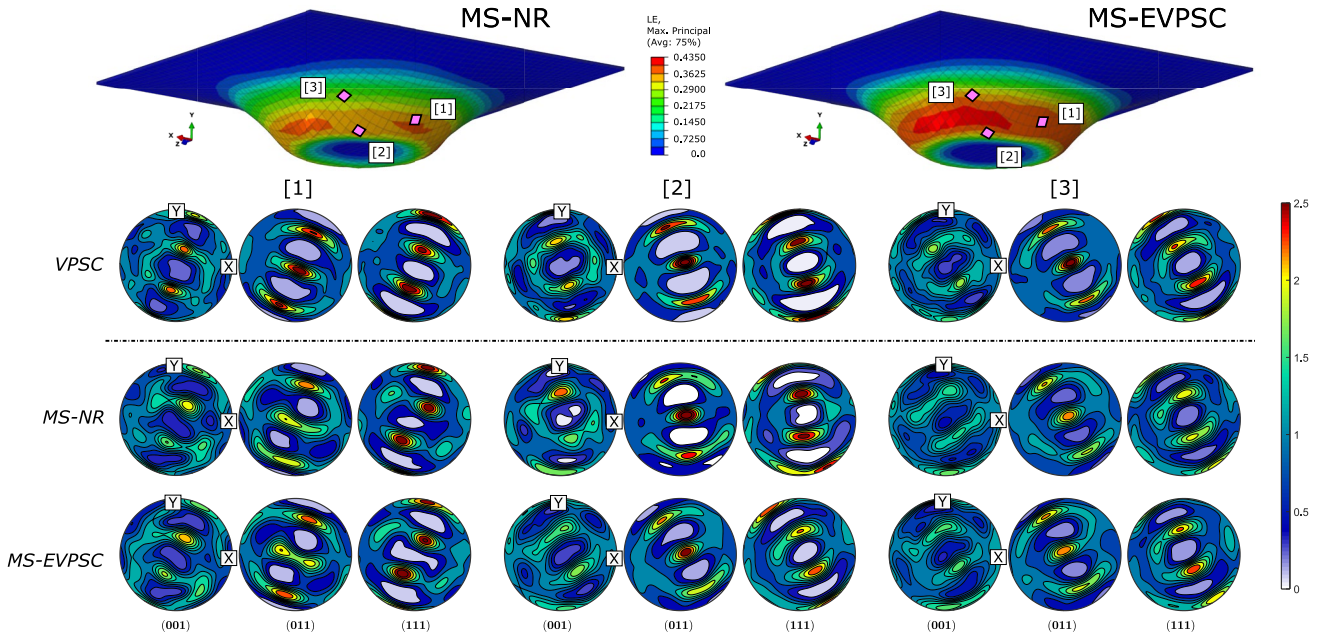

Fig. 13 Microscale texture results for truncated cone at various material points using the base VPSC, MS-NR, and MS-EVPSC models

simulation aligned with the timesteps at which the tool changed direction along the square tool path, whereas the truncated cone tool path showed a less noisy response along its circular path.

Overall, force profiles for both models for each geometry were similar in shape but showed differences up to 7% for the pyramid tool path and up to 16% of for the cone tool path. For both tool paths, the forming forces for the MS-EVPSC model were lower than those of the MS-NR model. Better agreement between macroscopic forces was observed during earlier parts of the simulation and deviation increased as simulation time increased.

Table 2 Computational cost in CPU hours of multiscale workflows including cost of data generation, training, and finite element analysis

	Concurrent model	MS-NR	MS-EVPSC
Data generation: ML-VPSC	–	805	805
Training: ML-VPSC	–	160	160
Data generation: ML-EVPSC	–	–	1750
Training: ML-EVPSC	–	–	415
Surrogate Modeling Cost	–	*965*	*3130*
FEA simulation [CPU hr]	**9540**	**2865**	**150**
Full Cost of 1 sim.	*9540*	*3830*	*3280*
Full Cost of 5 sim.	*47,700*	*15,290*	*3880*

Texture

Plastic strain histories from particular points of interest in formed geometries were input into ML-Tex to evaluate differences in texture prediction for each model. Plastic strains were directly computed during the NR procedure in the MS-NR model, and were extracted using Hooke's Law and total strain and stresses in the MS-EVPSC model.

Figure 12 shows the texture results at various points of interest for the truncated pyramid tool path and Fig. 13 shows the microstructural texture results for the same points in the truncated cone tool path. These points were chosen as the same elements across geometries and include points of high strain in both geometries (cone: point [1], pyramid: point [2]) and a point at the corner of the pyramid tool path (point [3]). The plastic strain histories at these points were input into the base VPSC model, and comparison of textures are shown for the VPSC, MS-NR, and MS-EVPSC models.

Both the MS-NR and MS-EVPSC models show good agreement of texture with the VPSC model for all material points in both geometries. The largest differences were observed at points with stronger textures and higher intensities. However, the qualitative texture trends are captured well. Plastic strain histories at these points were characterized by thinning along the thickness direction, stretching along the wall, and some amounts of shear. The textures observed are similar in nature to the 'plane strain with shear' deformation path used for validation of the surrogate models. The performance on the validation path

as well as comparison to ground truth provide validation of ML-Tex for the deformations present in SPIF.

Computational Cost

Table 2 shows the computational cost of the multiscale workflows including data generation and training for surrogate models and cost of multiscale FE model evaluation. As ML-VPSC was used to generate training data for ML-EVPSC, the "Surrogate Modeling" cost includes generation of both data sets as well as training of both models. The full cost of a multiscale simulation includes "Surrogate Modeling" and "FEA Simulation" costs. Additionally, the net cost of a small trade study with 5 multiscale simulations is calculated and included.

The cost of a baseline concurrent multiscale model using VPSC was estimated using work by Prakash et al. [25]. The authors developed a multiscale model that used a NR approach with VPSC and an analytical form of the Jacobian which required 2–3 iterations per plastic update step. The cost of applying this approach was estimated by: extracting the number of FE timesteps at which the plastic update algorithm was called during the MS-NR SPIF simulations across all 800,000 timesteps and all 10,000 elements (pyramid $\approx 580,000,000$, cone $\approx 610,000,000$), assuming 2 iterations per timestep, and using the average cost per VPSC iteration of the training data (≈ 29 ms/iteration). Values in Table 2 are averaged between both geometry tool paths. The resulting computational speed up for the MS-NR model compared to a baseline VPSC concurrent model was 3.33x and the speedup for the MS-EVPSC model was 63.6x.

Computational efficiency can also be estimated for texture prediction. Evaluation of ML-Tex with 10,000 elements with 50 timesteps using a GPU took 2 s to evaluate. This would correspond to 10,000 individual CP simulations on VPSC which cost $\approx$ 8s for 50 timesteps, which gives a speedup factor of 40,000x.

Discussion

This work demonstrates an efficient multiscale FE analysis workflow using ML surrogate models of CP applied to SPIF. Surrogate models were developed for both texture evolution and CP constitutive response which enabled full-field texture evolution results over a formed part at a significantly decreased computational cost.

The use of embedded surrogate models for the constitutive response avoids the fitting and correlating of multiple models between the macroscale FE and microscale CP length scales performed in hierarchical approaches. Both multiscale workflows in this work showed good agreement between results for macroscopic and microscopic quantities. Overall, general macroscopic behaviors such as strain concentrations/profiles in the edges, center, and walls of the formed parts in Fig. 10, as well as trends for constant, increasing, and decreasing force values in Fig. 11 were matched in both models for both tool paths. Despite some differences in the magnitude of macroscopic strain contours, good agreement of texture prediction to the base VPSC model was also demonstrated for both tool paths as seen in Figs. 12 and 13 for high strain values within the simulation. While there is an inherent tradeoff between accuracy and cost when using surrogate models, the robustness of this approach demonstrates an appropriate accuracy for texture prediction of Al5052-H32 in SPIF. These efficient full-field CP simulations can ultimately support multiscale design optimization for targeted microstructures in a formed geometry, and enable trade studies for varying macroscale manufacturing parameters such as frictional effects, tool head geometry, and tool path.

A significant benefit of ML-Tex is the capability to take multi-sample inputs directly extracted from the SPIF simulation. While only shown for a few material points in Figs. 12 and 13, texture evolution is calculated for all elements of the SPIF formed part and contains information over the whole time history. If evaluated in the base VPSC model, this would correspond to 10,000 individual CP simulations (8 s/simulation) which would have been impractical to calculate. Instead, this is a single ML operation of very low cost (2 s/10,000 samples) which corresponds to a 40,000x speedup. We can then readily use this model by inputting values directly from SPIF results. While shown here for SPIF, ML-Tex has the capability to predict other deformation paths such as cyclic behavior and pure shear as seen in Fig. 9. This enables the general ability to capture the various deformation paths in SPIF but also illustrates the capability for paths from other macroscale boundary conditions. This enables full-field extraction of local texture information which can help explore the processing-structure–property relationship at material points to macroscale parameters in various metal manufacturing processes.

The low evaluation cost of surrogate models is underscored when comparing to established models and techniques, which certainly holds when utilizing previously defined datasets. However, for cases where surrogate models are used to replace expensive but uncommon models such as a particular CP system, manufacturing case, or load condition, the dataset must first be computed and therefore additional costs for data generation exist. In this work, we demonstrate how a surrogate model can be used as a means to efficiently produce additional training datasets for subsequent models. While this has implications in terms of the compounded error, we see good agreement between the baseline (VPSC) and final (ML-EVPSC) model through

comparison of the deviatoric stress responses in Fig. 5 (max deviation: 15 MPa) and Fig. 6 (max deviation: 4 MPa). Elastic–plastic samples of 2000 timesteps and lower signal-to-noise ratio were generated in 120 CPUsec (16 timesteps/s) compared to VPSC plastic data of 150 timesteps in 50 CPUsec (3 timesteps/s).

Lower prediction errors were observed during earlier timesteps and later increase in testing data (Figs. 5c-d, 6c-d), validation data (Figs. 5e-g, 6e-g), and macroscale forming forces (Fig. 11). A possible explanation is the increased space spanned by the strain bounds at those limits, which leads to a sparser dataset and less information for learning. Data generation in the form of many smoothly varying strain paths in Fig. 3 has been successfully demonstrated in this work for texture evolution and constitutive response as well as in other literature [31, 32, 47]. While better coverage of the strain space could be attained by generation of more samples, it would be more effectively covered by generation of *intentional* samples. For example, noise in elastic–plastic data, low strain elastic–plastic values, and plane strain deformation paths for plastic data were considered in this work as intentional data. Intentional elastic–plastic data showed improved predictions of lower strains in the edges and center of formed geometries, and plane strain plastic data showed better agreement in validation plots. Future work may entail more rigorous investigation of intentional data common to particular manufacturing techniques or load cases. Other approaches such as active learning [48] are promising to explore for determining the nature and amount of data needed to attain particular accuracy as well.

As it stands, this work is implemented for a single material system of an Al5052-H32 material with non-varying elastic constants. Applications to other materials would require generation of additional datasets and re-training of the models. Additionally, while we have demonstrated reduced-order representation of texture for FCC crystal structures, more work is required to extend to systems of lower symmetry. However, the generalized approach of these workflows can be readily applied to other material systems using tools developed in this work. Such tools include data generation scripts which are parallelizable on a high performance cluster and decreases the wall time needed to produce a multiscale model. Current literature has also investigated the use of transfer learning for surrogate models of the constitutive response [49] which could offer potential to adapt trained surrogate models with other crystal plastic models and distinct material systems (such as HCP or BCC).

Conclusions

This study focuses on development of computationally efficient multiscale CP simulations of SPIF using low-cost ML surrogate models. Two multiscale simulation workflows are developed using three ML surrogate models for the constitutive response and texture evolution of Al5052-H32. This work demonstrates a general workflow that can be applied to various material systems and manufacturing processes, which facilitates manufacturing process trade studies and full-field optimization of microstructure. The following conclusions are drawn:

- A generalized workflow for concurrent multiscale CP simulations using ML surrogate models permits evaluation of full-field time history texture response for various tool paths in SPIF.
- Surrogate models using RNNs for the constitutive response and texture evolution can significantly decrease the computational cost of concurrent multiscale CP simulations of SPIF up to 63.6x, and evaluation of full-field texture prediction up to 40,000x compared to isolated CP simulations.
- Reduced order representation of texture using harmonic coefficients and PCA allows ML of texture evolution with sufficient accuracy.
- Datasets spanning appropriate set spaces (varying strain path history, inclusion of noise) allow generalized behavior of CP surrogate models and can be used in both constitutive response and texture evolution.
- Computational cost of dataset generation for an elastic-crystal plastic response can be decreased by using a surrogate model for the crystal plastic response.
- This framework demonstrates feasibility for efficient multiscale CP simulations of other metal forming processes with varying deformation histories including incremental processes and conventional techniques (rolling, forging, etc.).

The current framework has been demonstrated for a random textured Al5052-H32 material but future work may include implementation of this model with rolled textures, as well as other material systems, which would allow further investigation of the effects of microstructure and local properties in incremental forming. Future work also includes experimental comparisons to forming force, resultant geometry, and texture prediction for this process. This would include manufacturing using a SPIF set-up for the studied geometries and characterization of texture at multiple points of interest using techniques such as electron backscatter and x-ray diffraction.

Full-field relations between manufacturing parameters and texture could also enable local microstructural optimization using macroscale manufacturing processing parameters and data-driven multiscale design. A particularly interesting research direction is that of autonomy in metal forming, such as decision making or real-time adjustment of manufacturing parameters toward targeted microstructures. Future work entails evaluating this relationship between texture and local properties for a particular material system, and developing a decision making process to target during manufacturing operations.

Editor's Video Summary The online version of this article (https://doi.org/10.1007/s40192-025-00427-0) contains an Editor's Video Summary, which is available to authorized users.

Acknowledgements Funding from the AI Manufacturing Pilot Facility project under Georgia Artificial Intelligence in Manufacturing (Georgia AIM) provided by the Economic Development Administration, award 04-79-07808 is acknowledged.

Data Availability Code and data that support the findings of this study are openly available from Zenodo at https://doi.org/10.5281/zenodo.17058561.

Declarations

Conflict of interest On behalf of all authors, the corresponding author states that there is no conflict of interest.

References

1. Spanos G, Daehn G, Allison J, Bilitz E, Bourne D, Cao J, Clarke K, DeLoach Jr J, Herderick E, Lewandowski J et al (2019) Metamorphic manufacturing: Shaping the future of on-demand components. Technical report, The Minerals Metals & Materials Society. https://apps.dtic.mil/sti/citations/AD1070167
2. Horstemeyer MF (2012) Integrated computational materials engineering (ICME) for metals : using multiscale modeling to invigorate engineering design with science. John Wiley & Sons, Hoboken. https://doi.org/10.1002/9781118342664
3. Banabic D (ed.) (2016) Multiscale modelling in sheet metal forming. Springer, Cham. https://doi.org/10.1007/978-3-319-44070-5. http://www.springer.com/series/11923
4. Jeswiet J, Micari F, Hirt G, Bramley A, Duflou J, Allwood J (2005) Asymmetric single point incremental forming of sheet metal. CIRP Annal 54:88–114. https://doi.org/10.1016/S0007-8506(07)60021-3
5. Peng W, Ou H, Becker A (2019) Double-sided incremental forming: A review. J Manuf Sci Eng Trans ASME 141:050802. https://doi.org/10.1115/1.4043173
6. Smith J, Malhotra R, Liu WK, Cao J (2013) Deformation mechanics in single-point and accumulative double-sided incremental forming. Int J Adv Manuf Technol 69:1185–1201. https://doi.org/10.1007/s00170-013-5053-3
7. Darzi S, Kinsey BL, Ha J (2024) Reforming toolpath effect on deformation mechanics in double-sided incremental forming. Int J Mech Sci 280:109548. https://doi.org/10.1016/j.ijmecsci.2024.109548
8. Malhotra R, Xue L, Belytschko T, Cao J (2012) Mechanics of fracture in single point incremental forming. J Mater Proc Tech. 212:1573–1590. https://doi.org/10.1016/j.jmatprotec.2012.02.021
9. Li Y, Daniel WJT, Liu Z, Lu H, Meehan PA (2015) Deformation mechanics and efficient force prediction in single point incremental forming. J Mater Proc Technol 221:100–111. https://doi.org/10.1016/j.jmatprotec.2015.02.009
10. Lu B, Fang Y, Xu DK, Chen J, Ai S, Long H, Ou H, Cao J (2015) Investigation of material deformation mechanism in double side incremental sheet forming. Int J Mach Tools Manuf 93:37–48. https://doi.org/10.1016/j.ijmachtools.2015.03.007
11. Peng W, Ou H (2023) Deformation mechanisms and fracture in tension under cyclic bending plus compression, single point and double-sided incremental sheet forming processes. Int J Mach Tools Manuf 184:103980. https://doi.org/10.1016/j.ijmachtools.2022.103980
12. Asaro RJ (1983) Crystal plasticity. J Appl Mech 50:921–934. https://doi.org/10.1115/1.3167205
13. Kalidindi SR, Bronkhorst CA, Anand L (1992) Crystallographic texture evolution in bulk deformation processing of FCC metals. J Mech Phys Solids 40:537–569. https://doi.org/10.1016/0022-5096(92)80003-9
14. Roters F, Eisenlohr P, Bieler TR, Raabe D (2010) Crystal plasticity finite element methods in materials science and engineering. Wiley-VCH, Weinheim, Germany. https://doi.org/10.1002/9783527631483
15. Hill R (1948) A theory of the yielding and plastic flow of anisotropic metals. Proc Royal Soc London Series Mathe Phys Sci 193(1033):281–297. https://doi.org/10.1098/rspa.1948.0045
16. Cazacu O, Plunkett B, Barlat F (2006) Orthotropic yield criterion for hexagonal closed packed metals. Int J Plasticity 22:1171–1194. https://doi.org/10.1016/j.ijplas.2005.06.001
17. Esmaeilpour R, Kim H, Park T, Pourboghrat F, Xu Z, Mohammed B, Abu-Farha F (2018) Calibration of Barlat Yld2004-18P yield function using CPFEM and 3D RVE for the simulation of single point incremental forming (SPIF) of 7075-O aluminum sheet. Int J Mech Sci 145:24–41. https://doi.org/10.1016/j.ijmecsci.2018.05.015
18. Esmaeilpour R, Kim H, Asgharzadeh A, Tiji SAN, Pourboghrat F, Banu M, Bansal A, Taub A (2021) Experimental validation of the simulation of single-point incremental forming of AA7075 sheet with Yld2004-18P yield function calibrated with crystal plasticity model. Int J Adv Manuf Technol 113:2031–2047. https://link.springer.com/article/10.1007/s00170-021-06706-2
19. Mishra S, Yazar KU, More AM, Kumar L, Lingam R, Reddy NV, Prakash O, Suwas S (2020) Elucidating the deformation modes in incremental sheet forming process: Insights from crystallographic texture, microstructure and mechanical properties. Mater Sci Eng A 790:139311. https://doi.org/10.1016/j.msea.2020.139311
20. Tomé CN, Lebensohn R (2023) Material modeling with the visco-plastic self-consistent (VPSC) approach. Elsevier, Cambridge. https://doi.org/10.1016/b978-0-12-820713-0.00013-8

21. Rakshit R, Katiyar BS, Tomé CN, Panda SK, Mandal S (2023) A finite element coupled visco-plastic self-consistent simulation to predict micro-texture and anisotropy evolution during single point incremental forming in al-li alloy. J Mater Proc Technol 312:117834. https://doi.org/10.1016/j.jmatprotec.2022.117834
22. Segurado J, Lebensohn RA, Llorca J (2018) Computational homogenization of polycrystals. Adv Appl Mech 51:1–114. https://doi.org/10.1016/bs.aams.2018.07.001
23. Segurado J, Lebensohn RA, Llorca J, Tomé CN (2012) Multiscale modeling of plasticity based on embedding the viscoplastic self-consistent formulation in implicit finite elements. Int J Plasticity 28:124–140. https://doi.org/10.1016/j.ijplas.2011.07.002
24. Walde T, Riedel H (2007) Simulation of earing during deep drawing of magnesium alloy AZ31. Acta Materialia 55:867–874. https://doi.org/10.1016/j.actamat.2006.09.007
25. Prakash A, Nöhring WG, Lebensohn RA, Höppel HW, Bitzek E (2015) A multiscale simulation framework of the accumulative roll bonding process accounting for texture evolution. Mater Sci Eng A 631:104–119. https://doi.org/10.1016/j.msea.2015.02.005
26. Cao J, Bambach M, Merklein M, Mozaffar M, Xue T (2024) Artificial intelligence in metal forming. CIRP Annals 73:561–587. https://doi.org/10.1016/j.cirp.2024.04.102
27. Mozaffar M, Bostanabad R, Chen W, Ehmann K, Cao J, Bessa MA (2019) Deep learning predicts path-dependent plasticity. Proc Nat Acad Sci 116:26414–26420. https://doi.org/10.1073/pnas.1911815116
28. Gorji MB, Mozaffar M, Heidenreich JN, Cao J, Mohr D (2020) On the potential of recurrent neural networks for modeling path dependent plasticity. J Mech Phys Solids 143:103972. https://doi.org/10.1016/j.jmps.2020.103972
29. Logarzo HJ, Capuano G, Rimoli JJ (2021) Smart constitutive laws: Inelastic homogenization through machine learning. Comp Meth Appl Mech Eng 373:113482. https://doi.org/10.1016/j.cma.2020.113482
30. Bonatti C, Mohr D (2022) On the importance of self-consistency in recurrent neural network models representing elasto-plastic solids. J Mech Phys Solids 158:104697. https://doi.org/10.1016/j.jmps.2021.104697
31. Liu B, Ocegueda E, Trautner M, Stuart AM, Bhattacharya K (2023) Learning macroscopic internal variables and history dependence from microscopic models. J Mech Phys Solids 178:105329. https://doi.org/10.1016/j.jmps.2023.105329
32. Bonatti C, Berisha B, Mohr D (2022) From CP-FFT to CP-RNN: Recurrent neural network surrogate model of crystal plasticity. Int J Plasticity 158:103430. https://doi.org/10.1016/j.ijplas.2022.103430
33. Yuan M, Paradiso S, Meredig B, Niezgoda SR (2018) Machine learning-based reduce order crystal plasticity modeling for ICME applications. Integr Mater Manuf Innov 7:214–230. https://doi.org/10.1007/s40192-018-0123-x
34. Ali U, Muhammad W, Brahme A, Skiba O, Inal K (2019) Application of artificial neural networks in micromechanics for polycrystalline metals. Int J Plasticity 120:205–219. https://doi.org/10.1016/j.ijplas.2019.05.001
35. Ibragimova O, Brahme A, Muhammad W, Lévesque J, Inal K (2021) A new ANN based crystal plasticity model for FCC materials and its application to non-monotonic strain paths. Int J Plasticity 144:103059. https://doi.org/10.1016/j.ijplas.2021.103059
36. Chapuis A, Liu Q (2018) Effect of strain rate sensitivity in visco-plastic modeling. Int J Solids Struct 152–153:217–227. https://doi.org/10.1016/j.ijsolstr.2018.06.029
37. Bachmann F, Hielscher R, Schaeben H (2010) Texture analysis with MTEX – free and open source software toolbox. In: Texture and anisotropy of polycrystals III. solid state phenomena, vol. 160, pp. 63–68. Trans Tech Publications Ltd, Switzerland. https://doi.org/10.4028/www.scientific.net/SSP.160.63
38. Chen X, Peng Y, Chen C, Li J, Wang K, Wang T (2019) Mechanical behavior and texture evolution of aluminum alloys subjected to strain path changes: Experiments and modeling. Mater Sci Eng A 757:32–41. https://doi.org/10.1016/j.msea.2019.04.091
39. Bower AF (2009) Applied mechanics of solids, 1st edn. CRC Press, Boca Raton, USA. https://doi.org/10.1201/9781439802489
40. Kingma DP, Ba J (2014) Adam: A method for stochastic optimization. arXiv preprint arXiv:1412.6980
41. Lingam R, Bansal A, Reddy NV (2016) Analytical prediction of formed geometry in multi-stage single point incremental forming. Int J Mater Form 9:395–404. https://doi.org/10.1007/s12289-015-1226-y
42. Mugendiran V, Gnanavelbabu A (2014) Comparison of FLD and thickness distribution on aa5052 aluminium alloy formed parts by incremental forming process. Proced Eng 97:1983–1990. https://doi.org/10.1016/j.proeng.2014.12.353
43. Bhattacharya A, Maneesh K, Reddy NV, Cao J (2011) Formability and surface finish studies in single point incremental forming. J Manuf Sci Eng 133:061020. https://doi.org/10.1115/1.4005458
44. Rasmussen CE, Williams CKI (2006) Gaussian processes for machine learning. MIT Press, Cambridge, USA. www.GaussianProcess.org/gpml
45. Bunge HJ (1982) Texture analysis in materials science: mathematical methods. Butterworths and Co, Germany. https://doi.org/10.1016/B978-0-408-10642-9.50001-5
46. Eghtesad A, Barrett TJ, Knezevic M (2018) Compact reconstruction of orientation distributions using generalized spherical harmonics to advance large-scale crystal plasticity modeling: Verification using cubic, hexagonal, and orthorhombic polycrystals. Acta Materialia 155:418–432. https://doi.org/10.1016/j.actamat.2018.06.017
47. Liu B, Kovachki N, Li Z, Azizzadenesheli K, Anandkumar A, Stuart AM, Bhattacharya K (2022) A learning-based multiscale method and its application to inelastic impact problems. J Mech Phys Solids 158:104668. https://doi.org/10.1016/j.jmps.2021.104668
48. Settles B (2009) Active learning literature survey. Technical report, University of Wisconsin-Madison Department of Computer Sciences. http://digital.library.wisc.edu/1793/60660
49. Heidenreich JN, Mohr D (2024) Recurrent neural network plasticity models: Unveiling their common core through multi-task learning. Comp Meth Appl Mech Eng 426:116991. https://doi.org/10.1016/j.cma.2024.116991